

OPTIMIZED TRAJECTORY CORRECTION BURN PLACEMENT FOR THE NASA ARTEMIS II MISSION

David Woffinden*, Randy Eckman†, Shane Robinson‡

The NASA Artemis II mission represents the first time humans plan to return to the lunar vicinity in over 50 years with a crew traveling to the Moon in the Orion spacecraft on a free return trajectory. This first crewed mission of the Artemis program will evaluate human-rated elements of Orion in preparation to sending astronauts to the lunar surface. The selected free-return cislunar trajectory profile that is reminiscent of the Apollo 8 mission that nominally requires no additional translational burns following the trans-lunar injection (TLI) burn. Due to crew activity, maneuver execution errors, navigation uncertainty, orbit insertion errors, disturbance accelerations, and other system limitations; periodic trajectory correction burns are necessary to ensure proper entry interface (EI) conditions are satisfied for a safe return to Earth. Robust trajectory optimization techniques are utilized to determine the optimized placements for the Artemis II trajectory correction burns that accounts for the crew schedule, both the primary and backup navigation systems, targeting strategies and burn plan configurations, spacecraft venting, thruster selection, and the integrated GN&C performance.

INTRODUCTION

In NASA's preparations to return humans to the lunar surface and other destinations in the solar system, the Artemis II mission represents the first time in over 50 years NASA plans to send astronauts to the lunar vicinity. This first crewed mission of the Artemis program will evaluate human-related elements of the Orion spacecraft that are vital to support upcoming exploration efforts. As illustrated in Figure 1, the selected free-return cislunar trajectory profile for Artemis II is reminiscent of the Apollo 8 mission that does not require additional translational burns following the trans-lunar injection (TLI) burn under nominal conditions. However, due to crew activity, maneuver execution errors, navigation uncertainty, orbit insertion errors, disturbance accelerations acting on the spacecraft, and other system limitations; periodic trajectory correction burns are necessary to ensure proper entry interface (EI) conditions are satisfied for a safe return to Earth.

This work begins investigating the optimized placement of these trajectory correction burns that accounts for uncertainty in the system, the dynamics of the cis-lunar transfer, the geometry of the utilized sensor measurements from the ground tracking stations of the primary navigation system along with the geometry of the Earth and Moon for the backup optical navigation system, the crew schedule, spacecraft venting, targeting and burn plan configurations, thruster selection, and the complex interaction of the overall integrated guidance, navigation, and control (GN&C) system. Robust trajectory optimization techniques are adopted to solve this comprehensive problem which utilizes

*Aerospace Engineer, GN&C Autonomous Flight Systems Branch, NASA Johnson Space Center, Houston TX, 77058

†Aerospace Engineer, Flight Mechanics and Trajectory Design Branch, NASA Johnson Space Center, Houston TX, 77058

‡Aerospace Engineer, GN&C Autonomous Flight Systems Branch, NASA Johnson Space Center, Houston TX, 77058

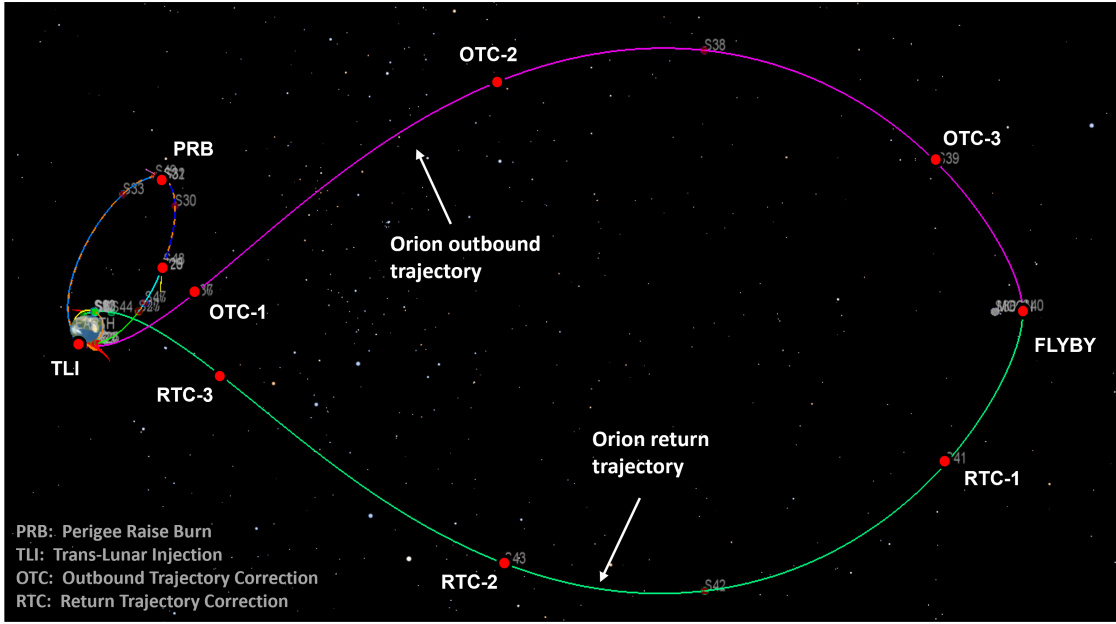


Figure 1. Notional Orion Free-Return Trajectory for the NASA Artemis II Mission

linear covariance (LinCov) analysis^{1,2} interfaced with a genetic algorithm (GA). The objective is to minimize the total 3-sigma delta-v usage while constraining the entry interface trajectory dispersions to remain within the allocated performance specifications.

The use of these non-traditional robust trajectory optimization or robust trajectory design techniques were originally developed and demonstrated for rendezvous applications in low Earth orbit.³ It was then extended to cis-lunar outbound trajectories to an NRHO⁴ and introduced for a simple rendezvous approach trajectory in the NRHO for mid-course correction placement.⁵ Recently, these robust trajectory optimization principles have been applied to solve cislunar transfers to low-lunar orbit,⁶ NRHO rendezvous and docking,⁷ lunar powered descent and landing,⁸ along with Mars aerocapture⁹ problems. They are currently being exercised to also determine the optimized trajectory correction burn placement for NRHO orbit maintenance anticipated for the Artemis III mission.¹⁰ This work applies these same principles to the NASA Artemis II trajectory to identify the location of both the outbound trajectory correction (OTC) burns as well as the return trajectory correction (RTC) burns.

ANALYSIS APPROACH

Performance Metrics

To optimize the performance of Artemis II trajectory corrections to system uncertainty, there are several performance metrics that are utilized which include the true trajectory dispersions $\delta\mathbf{x}$, the navigation dispersions $\delta\hat{\mathbf{x}}$, the true navigation error $\delta\mathbf{e}$, and the onboard navigation error $\delta\hat{\mathbf{e}}$ as depicted in Figure 2. The true dispersions $\delta\mathbf{x}$ are defined as the difference between the true state \mathbf{x} and the nominal state $\bar{\mathbf{x}}$. The true state \mathbf{x} is an n -dimensional vector that represents the *real world* environment or actual state.

$$\delta\mathbf{x} \triangleq \mathbf{x} - \bar{\mathbf{x}} \quad \mathbf{D} = E[\delta\mathbf{x}\delta\mathbf{x}^T] \quad (1)$$

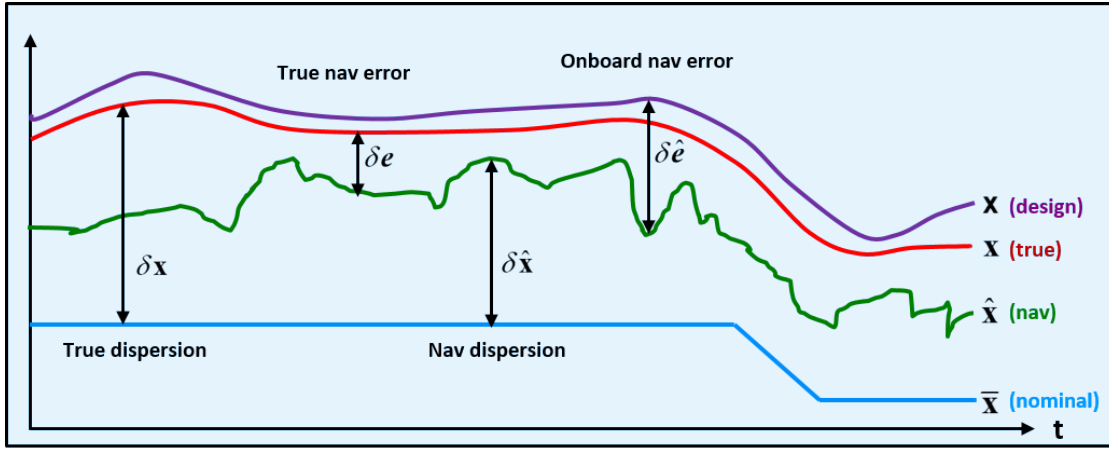


Figure 2. GN&C Performance Metric Variables

The nominal state \bar{x} is also an n -dimensional vector that represents the desired or reference state. The covariance of the environment dispersions, \mathbf{D} , indicates how precisely the system can follow a desired trajectory.

The navigation dispersions $\delta\hat{x}$ are defined as the difference between the navigation state \hat{x} and the nominal state \bar{x} . The navigation state is an \hat{n} -dimensional vector ($\hat{n} < n$) that represents the filter's estimated state.

$$\delta\hat{x} \triangleq \hat{x} - \mathbf{M}_x \bar{x} \quad \hat{\mathbf{D}} = E [\delta\hat{x}\delta\hat{x}^T] \quad (2)$$

The matrix \mathbf{M}_x is an $(\hat{n} \times n)$ matrix that maps the estimated state in terms of the true and nominal state. The covariance of the navigation dispersions, $\hat{\mathbf{D}}$, reflect how precisely the onboard system thinks it can follow a prescribed reference trajectory.

The true navigation error δe is the difference between the environment and navigation states. It is also the difference between the environment and the navigation dispersions.

$$\delta e \triangleq \mathbf{M}_x x - \hat{x} = \mathbf{M}_x \delta x - \delta\hat{x} \quad \mathbf{P} = E [\delta e \delta e^T] \quad (3)$$

The covariance of the true navigation error, \mathbf{P} , quantifies how precisely the onboard navigation system can estimate the actual state.

The onboard navigation error $\delta\hat{e}$ itself is never computed, but it is used to develop the onboard navigation filter equations. It is defined as the difference between the design state, x , and the navigation state \hat{x} .

$$\delta\hat{e} \triangleq x - \hat{x} \quad \hat{\mathbf{P}} = E [\delta\hat{e}\delta\hat{e}^T] \quad (4)$$

The covariance of the onboard navigation error, $\hat{\mathbf{P}}$, quantifies how precisely the onboard navigation system expects it can determine the actual state. The performance of the onboard navigation system is determined by comparing $\hat{\mathbf{P}}$ to the actual navigation performance \mathbf{P} . If the *true* states and the *design* states are assumed to be the same, then the true navigation covariance will equal the onboard navigation covariance.

The covariances of the true dispersions, navigation dispersions, true navigation error, and the onboard navigation error are ultimately used to analyze and assess the performance of a proposed GN&C system. A common approach to obtain these performance metrics is to use a Monte Carlo simulation outlined in Figure 3, where the sample statistics of hundreds or thousands of runs, N , are used to numerically compute the desired covariance matrices.

$$\mathbf{D} = \frac{1}{N-1} \sum \delta \mathbf{x} \delta \mathbf{x}^T \quad \hat{\mathbf{D}} = \frac{1}{N-1} \sum \delta \hat{\mathbf{x}} \delta \hat{\mathbf{x}}^T \quad \mathbf{P} = \frac{1}{N-1} \sum \delta \mathbf{e} \delta \mathbf{e}^T \quad (5)$$

The onboard navigation error covariance $\hat{\mathbf{P}}$ is the navigation filter covariance for each run. This same statistical information can be obtained using linear covariance analysis techniques.

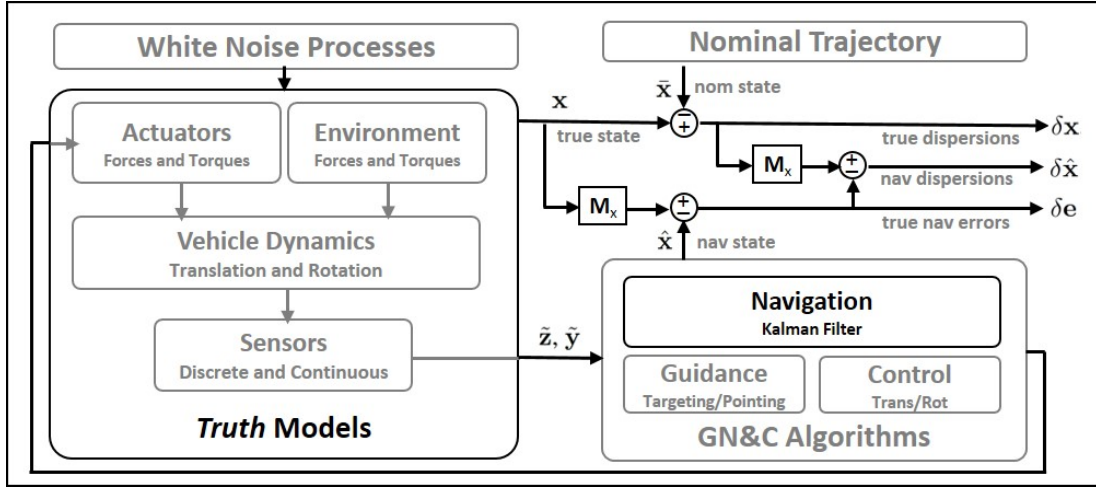


Figure 3. Extracting GN&C Performance Metrics Using Monte Carlo Techniques

Linear covariance analysis incorporates the non-linear system dynamics models and GN&C algorithms to generate a nominal reference trajectory $\bar{\mathbf{x}}$ which is then used to propagate, update, and correct an onboard navigation covariance matrix $\hat{\mathbf{P}}$ and an augmented state covariance matrix \mathbf{C} ,

$$\mathbf{C} = E [\delta \mathbf{X} \delta \mathbf{X}^T] \quad (6)$$

where the augmented state $\delta \mathbf{X}^T = [\delta \mathbf{x}^T \ \delta \hat{\mathbf{x}}^T]$ consists of the true dispersions and the navigation dispersions. Pre- and post-multiplying the augmented state covariance matrix by the following mapping matrices, the covariances for the trajectory dispersions, navigation dispersions, and the navigation error can be obtained.

$$\begin{aligned} \mathbf{D} &= [\mathbf{I}_{n \times n}, \mathbf{0}_{n \times \hat{n}}] \mathbf{C} [\mathbf{I}_{n \times n}, \mathbf{0}_{n \times \hat{n}}]^T \\ \hat{\mathbf{D}} &= [\mathbf{0}_{\hat{n} \times n}, \mathbf{I}_{\hat{n} \times \hat{n}}] \mathbf{C} [\mathbf{0}_{\hat{n} \times n}, \mathbf{I}_{\hat{n} \times \hat{n}}]^T \\ \mathbf{P} &= [\mathbf{I}_{\hat{n} \times n}, -\mathbf{I}_{\hat{n} \times \hat{n}}] \mathbf{C} [\mathbf{I}_{\hat{n} \times n}, -\mathbf{I}_{\hat{n} \times \hat{n}}]^T \end{aligned} \quad (7)$$

Linear Covariance Analysis

The linear covariance analysis equations used to propagate, update, and correct both the augmented state covariance matrix and the onboard navigation covariance matrix are summarized here along with the LinCov analysis inputs. For additional details regarding the development and implementation of the linear covariance simulation, see the following references.^{1, 2, 11, 12, 13, 14}

LinCov Analysis Modeling The discrete-time propagation equations for augmented state covariance matrix \mathbf{C} and the onboard navigation covariance matrix $\hat{\mathbf{P}}$ are

$$\mathbf{C}(t_{k+1}) = \mathbf{\Phi}(t_{k+1}, t_k)\mathbf{C}(t_k)\mathbf{\Phi}^T(t_{k+1}, t_k) + \mathbf{G}\mathbf{Q}\mathbf{G}^T \quad (8)$$

$$\hat{\mathbf{P}}(t_{k+1}) = \hat{\mathbf{\Phi}}(t_{k+1}, t_k)\hat{\mathbf{P}}(t_k)\hat{\mathbf{\Phi}}^T(t_{k+1}, t_k) + \hat{\mathbf{G}}\hat{\mathbf{Q}}\hat{\mathbf{G}}^T \quad (9)$$

where $\mathbf{\Phi}$ and $\hat{\mathbf{\Phi}}$ are augmented and onboard state transition matrices respectively for the linearized perturbation dynamics about the reference trajectory. The mapping matrices, \mathbf{G} and $\hat{\mathbf{G}}$, are used to map environmental and navigation process noise characterized by \mathbf{Q} and $\hat{\mathbf{Q}}$, into \mathbf{C} and $\hat{\mathbf{P}}$.

The measurement update equations for augmented and navigation state covariance matrices, \mathbf{C} and $\hat{\mathbf{P}}$, at a measurement time t_i are

$$\mathbf{C}^+(t_i) = \mathbf{A}\mathbf{C}^-(t_i)\mathbf{A}^T + \mathbf{B}\mathbf{R}^j(t_i)\mathbf{B}^T \quad (10)$$

$$\hat{\mathbf{P}}^+(t_i) = \left[\hat{\mathbf{I}} - \hat{\mathbf{K}}^j(t_i)\hat{\mathbf{H}}^j \right] \hat{\mathbf{P}}^-(t_i) \left[I - \hat{\mathbf{K}}^j(t_i)\hat{\mathbf{H}}^j \right]^T + \hat{\mathbf{K}}^j(t_i)\hat{\mathbf{R}}^j(t_i)\hat{\mathbf{K}}^j(t_i)^T \quad (11)$$

where the superscript ‘ j ’ denotes the j th measurement type. The Kalman gain is written as

$$\hat{\mathbf{K}}^j(t_i) = \hat{\mathbf{P}}(t_i)(\hat{\mathbf{H}}^j)^T \left[\hat{\mathbf{H}}^j\hat{\mathbf{P}}^-(t_i)(\hat{\mathbf{H}}^j)^T + \hat{\mathbf{R}}^j(t_i) \right]^{-1} \quad (12)$$

The matrices $\hat{\mathbf{H}}$ and $\hat{\mathbf{R}}$ are the measurement sensitivity and measurement noise matrices respectively. The matrices \mathbf{A} and \mathbf{B} map the effects of the measurements and their associated noise to the navigation state dispersions.

The correction equations for \mathbf{C} and $\hat{\mathbf{P}}$ at a maneuver time t_m are

$$\mathbf{C}^+(t_m) = \mathbf{M}\mathbf{C}^-(t_m)\mathbf{M}^T + \mathbf{N}\mathbf{Q}_w^{act}\mathbf{N}^T \quad (13)$$

$$\hat{\mathbf{P}}^+(t_m) = \left[\hat{\mathbf{I}} + \hat{\mathbf{M}} \right] \hat{\mathbf{P}}^-(t_m) \left[I + \hat{\mathbf{M}} \right]^T + \hat{\mathbf{N}}\hat{\mathbf{Q}}_w^{act}\hat{\mathbf{N}}^T \quad (14)$$

The matrices \mathbf{M} and $\hat{\mathbf{M}}$ contain the control partials associated with a linearized two-impulse targeting algorithm. The matrices \mathbf{N} and $\hat{\mathbf{N}}$ are used to map the effects of actuator noise, described by \mathbf{Q}_w^{act} and $\hat{\mathbf{Q}}_w^{act}$, into \mathbf{C} and $\hat{\mathbf{P}}$.

Optimization Problem Formulation

For the Artemis II mission, top-level requirements exist to ensure the Orion spacecraft safely flies by the moon and returns the crew safely to Earth using the allocated propellant. For this analysis, the Orion spacecraft is not to come within 100 km of the lunar surface (the point of closest approach including dispersions must be greater than 100 km), utilize less than 20 m/s of delta-v for the outbound and return trajectory correction burns, and comply with the entry interface (EI) conditions that constrain the downtrack position, inertial velocity magnitude, inertial flight path angle, cross-track position, and cross-track velocity dispersions.^{15,16,17,18} Failure to comply with these EI requirements could severely impact the probability of mission success. A summary of these top-level constraints adopted for nominal Artemis II operations are illustrated in Figure 4 for the 3-sigma dispersions. For contingency scenarios the requirements are scaled by a factor of 2.5 and only the 2-sigma dispersions must comply with these degraded constraints.

Depending on the mission objectives and priorities, the optimization problem can be specified several different ways. For this study, three different problem formulations are evaluated which are

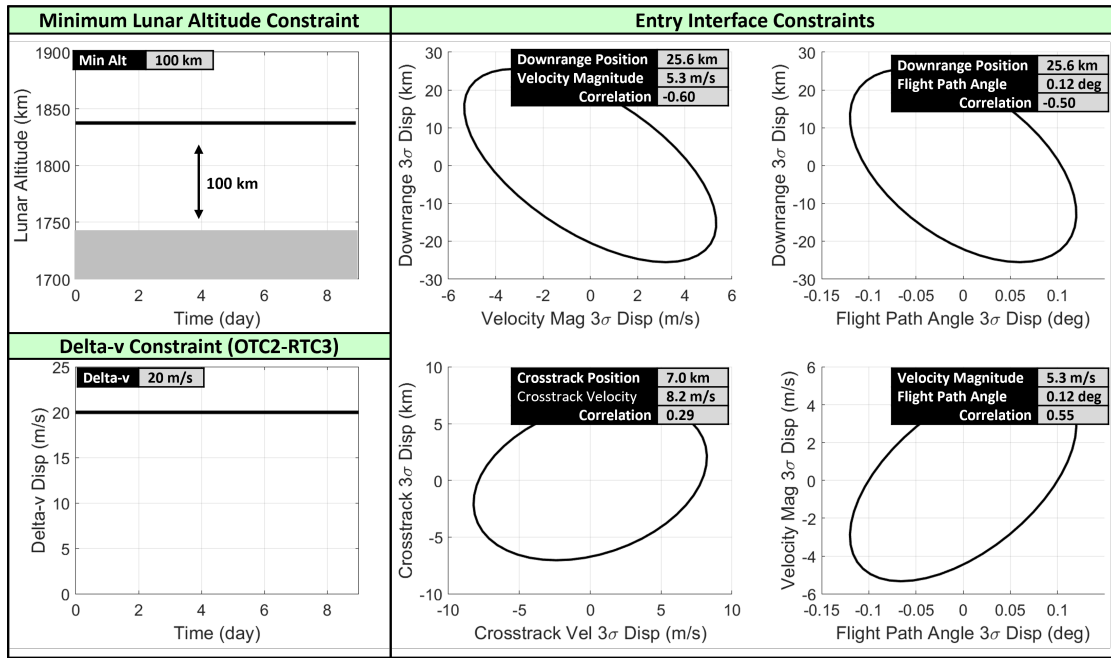


Figure 4. Notional Artemis II Lunar Altitude, Total Delta-v, and Entry Interface Constraints

defined in detail below as Problem #1 which strives to minimize the trajectory correction delta-v, Problem #2 which focuses on reducing entry interface dispersions, and Problem #3 which aims to reduce both delta-v and EI dispersions simultaneously. These quantities are extracted from the dispersion covariance, C along with other performance metrics.¹⁹

Other underlying constraints imposed in the optimization process is that the earliest a trajectory correction burn can occur is three hours after the trans-lunar injection (TLI) burn. The last RTC burn must be three hours prior to entry interface (EI). Both the OTC and the RTC burns must be separated from another by at least three hours and neither can occur within 1 hour of lunar flyby. The timing for the TLI burn and the first outbound trajectory correction (OTC1) are fixed such that only the burn times OTC2, OTC3, RTC1, RTC2, and RTC3 are optimized. For certain cases, if those burn times occur during the crew sleep period a violation penalty is added.

Problem #1 The first objective function, minimizes the total delta-v Δv_{total} which consists of the nominal plus 3-sigma delta-v dispersions from OTC2 to RTC3 subject to a constraint on the EI dispersions, lunar altitude dispersions, and burn times. For Problem #1, the constraints are implemented as a penalty function. If a constraint is violated, a large penalty κ is added to the objective function,

$$\text{minimize } (\Delta v_{total} + \kappa_{ei} + \kappa_{alt} + \kappa_{crew}) \quad (15)$$

where the penalty for violating the constraint for the EI dispersions κ_{ei} , the lunar flyby altitude dispersions κ_{alt} , and an operational penalty for performing a trajectory correction burn during the

crew sleep period κ_{crew} (if applied) are specified as,

$$\begin{aligned}
\Delta v_{total} &= \sum_{m=OTC2}^{RTC3} [\Delta \bar{v}(t_m) + 3\sigma_{\Delta v}(t_m)] \\
\sigma_{ei} &= -\sum_{n=1}^4 \frac{\sigma_{\delta ei}^{req}(n) - \sigma_{\delta ei}(n)}{\sigma_{\delta ei}^{req}(n)} * 100 \\
\kappa_{ei} &= \begin{cases} (1 \times 10^6) + \sigma_{ei}, & \text{if any } \sigma_{\delta ei} > \sigma_{\delta ei}^{req} \\ 0, & \text{otherwise} \end{cases} \\
\kappa_{alt} &= \begin{cases} (1 \times 10^6), & \text{if } \sigma_{\delta alt} > \sigma_{\delta alt}^{req} \\ 0, & \text{otherwise} \end{cases} \\
\kappa_{crew} &= \begin{cases} (1 \times 10^6), & \text{if activated and any burn is during crew sleep} \\ 0, & \text{otherwise} \end{cases}
\end{aligned}$$

Problem #2 The second objective function, minimizes the EI dispersions* σ_{ei} subject to constraints on the EI dispersions, total delta-v (nominal plus 3-sigma delta-v dispersions), the lunar flyby altitude dispersions, and burn times. The constraints are implemented as penalties to the cost function below,

$$\text{minimize } (\sigma_{\delta ei} + \kappa_{ei} + \kappa_{\Delta v} + \kappa_{alt} + \kappa_{crew}) \quad (16)$$

where the penalty for the lunar flyby altitude dispersions κ_{alt} and performing trajectory correction burn during the crew sleep period κ_{crew} (if applied) are defined previously. The total delta-v constraint violation $\kappa_{\Delta v}$ is specified as,

$$\kappa_{\Delta v} = \begin{cases} (1 \times 10^6) + \Delta v_{total}, & \text{if } \Delta v_{total} > 3\sigma_{\Delta v}^{req} \\ 0, & \text{otherwise} \end{cases}$$

Problem #3 The third objective function, simultaneously minimizes both the total delta-v and the EI dispersions subject to constraints on the EI dispersions, total delta-v, lunar flyby altitude dispersions, and burns times being outside the crew sleep period (if applied). The constraints are implemented as a penalty to the cost function below,

$$\text{minimize } (w_{\Delta v}\sigma_{\Delta v} + w_{ei}\sigma_{ei} + \kappa_{ei} + \kappa_{\Delta v} + \kappa_{alt} + \kappa_{crew}) \quad (17)$$

where the penalty for each violation are defined previously.

$$\begin{aligned}
\sigma_{dv} &= -\frac{\sigma_{dv}^{req} - \Delta v_{total}}{\sigma_{dv}^{req}} * 100 \\
\sigma_{ei} &= -\sum_{n=1}^4 \frac{\sigma_{\delta ei}^{req}(n) - \sigma_{\delta ei}(n)}{\sigma_{\delta ei}^{req}(n)} * 100 \\
w_{\Delta v} &= 100 * w, \text{ where } w = 0.75 \\
w_{\delta r} &= 100 * (1 - w)
\end{aligned}$$

*The EI dispersions are minimized by maximizing the margin for the EI requirements. Since the requirements are specified in terms of 2-dimensional covariance matrices, the margin is computed as outlined in the following reference¹⁹

LinCov Embedded in a Genetic Optimization Algorithm

Due to their complex nature, the optimization problem is solved using a genetic algorithm (GA). A genetic algorithm is a type of optimization solver which employs evolutionary processes to search a solution space.²⁰ A population of candidates is generated, evaluated, and based on their performance a new generation is created by combining and mutating them. During each iteration, candidate values of the optimization variables are passed to the LinCov simulation, which is then evaluated to determine the values of the cost and penalty functions. This process is summarized in Figure 5.

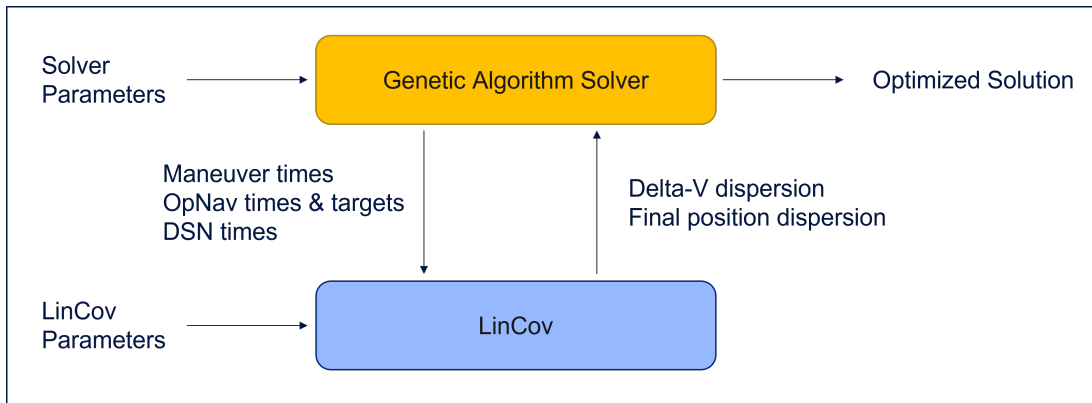


Figure 5. Functional relationship between the LinCov simulation and Genetic Algorithm.

For each of the optimization runs performed using the genetic algorithm, a population size of 60 was selected along with a maximum generation of 15. Both a larger population size and maximum number of generations are preferable, but due to run time limitations, the selected values provided a reasonable compromise between solution accuracy and speed to identify top level trends. Portions of the initial population are seeded with specific burn times related to the notional baseline configuration and other extreme conditions to ensure known corner cases are included as part of the solution.

GN&C MODELING

Following the trans-lunar injection (TLI) burn, the subsequent outbound trajectory correction (OTC) burns and the return trajectory correction (RTC) burns are nominally zero for the Artemis II free-return profile, regardless of when they are executed. The placement of the OTC and RTC burns do not impact the nominal performance, but they can have a significant influence in the integrated GN&C results when uncertainty in the system is included. Consequently, the optimization of the timing of the trajectory correction burns is driven by the implementation of the vehicle's GN&C system in context of the baseline Artemis II reference trajectory, the operational and crew time line, navigation modes, target configurations and burn plans, along with venting and disturbance acceleration modeling. This section contains the GN&C modeling assumptions and parameter specification that influences the optimized burn placement.

Nominal Artemis II Trajectory Profile and Time Line

An overview of the notional Artemis II trajectory profile is provided in Figure 6 where Figure 6(a) highlights the trajectory in the Earth/Moon rotating frame and Figure 6(b) shows the altitude profile as a function of time with the potential sensor measurement scheduling. The solid blue line represents the nominal reference trajectory with the solid red dots indicating major events such as translational burns. The thick black lines mark the designated crew sleep periods which consists of the pre-sleep, actual sleep, and post-sleep allocations.

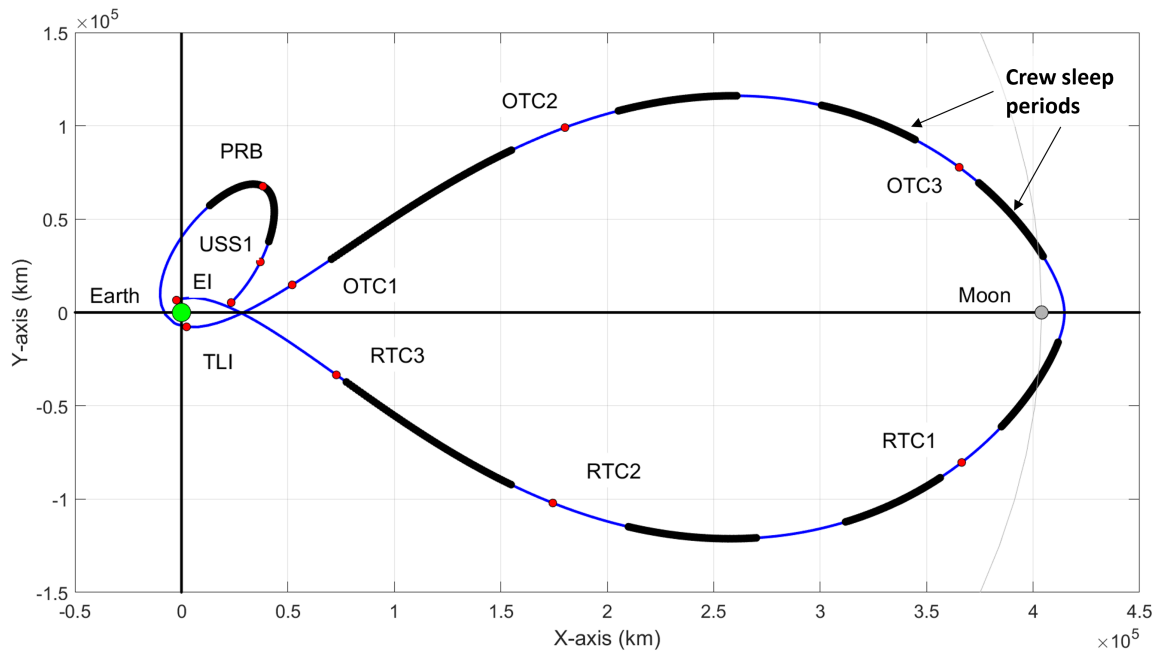
The scenario for this analysis starts in Earth orbit following an initial apogee raise burn (ARB) but about 2 hours prior to the upper stage separation (USS1) burn. Following USS1 and during the first crew sleep period, the perigee raise burn (PRB) is performed which is 12 hours prior to the trans-lunar injection (TLI) burn. TLI places Orion on a free-return trajectory that does a flyby of the moon about 4 days later and ultimately returning back to earth approximately 8 days following TLI. Three hours after TLI, the first outbound trajectory correction burn (OTC1) is scheduled. The baseline time line places the second OTC burn (OTC2) 24 hours after TLI and the third OTC burn (OTC3) is assumed to occur 24 hours prior to lunar flyby while avoiding the crew sleep period. As Orion begins its journey home, the first return trajectory correction burn (RTC1) is performed one day after lunar flyby. The last two return trajectory correction burns, RTC2 and RTC3, are executed both 21 hours and 5 hours prior to entry interface respectively. A summary of the timeline is provided in Table 1.

Table 1. Baseline Artemis II Time Line, Targeting, and Sensor Utilization

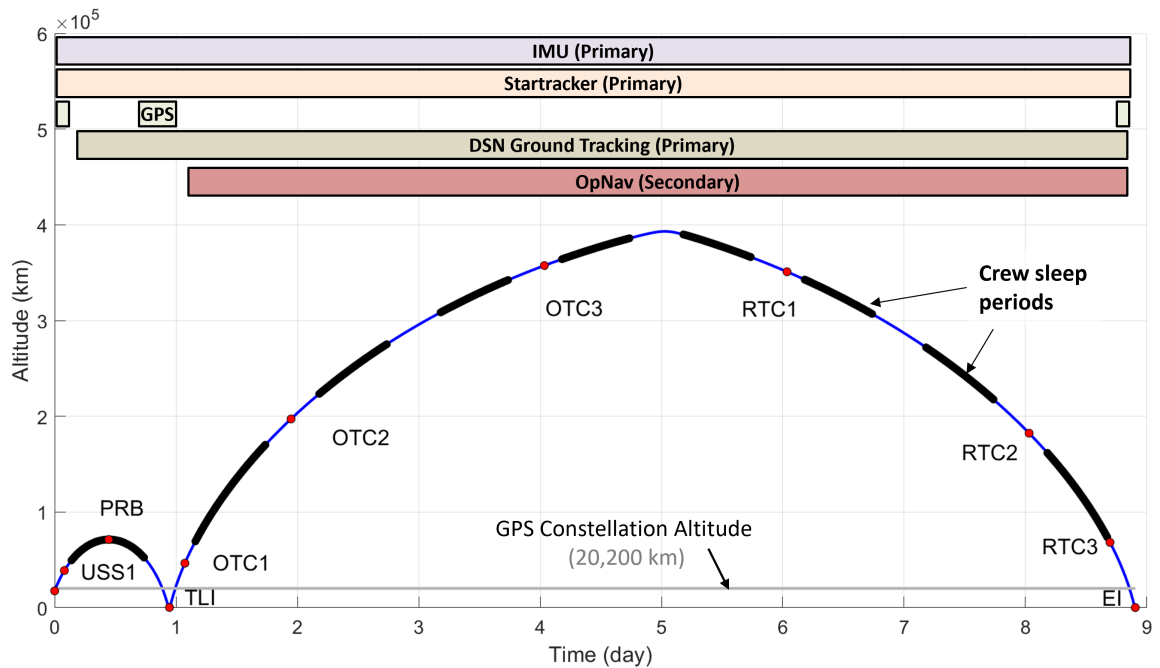
Event	Description	MET	Targ	Sensors
START	Post Apogee Raise Burn	0:00:00:00	—	IMU, Startracker, DSN, GPS
USS1	Upper Stage Separation Burn	0:01:55:34	TLT	IMU, Startracker, DSN
PRB	Perigee Raise Burn	0:10:41:34	TLT	IMU, Startracker, DSN
TLI	Trans-Lunar Injection Burn	0:22:42:09	TLT	IMU, Startracker, DSN, GPS
OTC1	Outbound Correction Burn #1	1:01:44:50	TLT	IMU, Startracker, DSN
OTC2	Outbound Correction Burn #2	1:22:44:50	TLT	IMU, Startracker, DSN (or OPNAV)
OTC3	Outbound Correction Burn #3	4:00:50:43	TLT	IMU, Startracker, DSN (or OPNAV)
FLYBY	Lunar Flyby	5:00:50:43	TLT	IMU, Startracker, DSN (or OPNAV)
RTC1	Return Correction Burn #1	6:00:50:43	TLT	IMU, Startracker, DSN (or OPNAV)
RTC2	Return Correction Burn #2	8:00:42:56	TLT	IMU, Startracker, DSN (or OPNAV)
RTC3	Return Correction Burn #3	8:16:42:56	TLT	IMU, Startracker, DSN (or OPNAV)
EI	Entry Interface	8:21:42:56	—	IMU, Startracker, DSN, GPS

As illustrated in Figure 6(b), from the initial USS1 burn through TLI, it is assumed that Orion is able to use a baseline navigation configuration which consists of IMU, startracker, GPS, and DSN ground tracking updates. When Orion's altitude is within the GPS constellation, GPS measurements are processed. Following OTC1, either the primary DSN ground tracking system or the secondary backup optical navigation (OpNav) system can be utilized to support the subsequent trajectory correction burns. In general, prior to each burn and afterwards, either a DSN ground estimate is uplinked to the spacecraft to support targeting and burn execution or an optical navigation (OpNav) pass is performed. This study assumes that the burn times and location for USS1 to OCT1

are fixed. The only burns that are modified to improve performance are OTC2 through RTC3. The simulation epoch is 2024 June 14 21:19:41 (or ET 771672050.59455 sec).



(a) Notional Artemis II trajectory overview in the Earth/Moon Rotating Frame with the baseline burn placement.



(b) Notional Artemis II altitude profile and sensor utilization

Figure 6. Notional Orion Artemis II Concept of Operations

Navigation System Modeling

Three different navigation systems are modeled for the trajectory correction burn placement analysis. The first represents a primary navigation system consisting of DSN ground updates, accelerometers, gyros, and star trackers. The second reflects a backup navigation system with an onboard optical navigation (OpNav) system along with accelerometers, gyros, and a star tracker. Lastly, to remove the impacts of the navigation errors on the trajectory correction burn placement analysis, a third navigation system is modeled referred to as *perfect nav*. For this navigation mode, the navigation errors are set to zero such that the navigation estimate equals the truth state. The mathematical models used for the different measurement types are provided below.

DSN Ground Update The Deep Space Network (DSN) ground update provides a position and velocity state estimate and covariance to the lander at designated epochs based on range $\tilde{\rho}$ and doppler measurements $\tilde{\dot{\rho}}$ between the ground tracking station and the spacecraft²¹ which are functions of the spacecraft's inertial position \mathbf{r}_l^i , the lander's mounted antenna location \mathbf{r}_a^b , lander's inertial-to-body transformation matrix \mathbf{T}_b^i , the lander's angular rate $\boldsymbol{\omega}_l^b$, the inertial-to-planet transformation \mathbf{T}_p^i , the Earth's angular rate $\boldsymbol{\omega}_e^p$, the ground station location \mathbf{r}_{gs}^p in the planet-fixed frame, the range bias b_ρ , doppler bias $b_{\dot{\rho}}$, range noise v_ρ , and doppler noise $v_{\dot{\rho}}$.

$$\tilde{\rho} = \left| \mathbf{r}_l^i + \mathbf{T}_b^i \mathbf{r}_a^b - \mathbf{T}_p^i \mathbf{r}_{gs}^p \right| + b_\rho + v_\rho \quad (18)$$

$$\tilde{\dot{\rho}} = \frac{[\mathbf{v}_l^i + \mathbf{T}_b^i (\boldsymbol{\omega}_l^b \times \mathbf{r}_a^b) - \mathbf{T}_p^i (\boldsymbol{\omega}_e^p \times \mathbf{r}_{gs}^p)]^T [\mathbf{r}_l^i + \mathbf{T}_b^i \mathbf{r}_a^b - \mathbf{T}_p^i \mathbf{r}_{gs}^p]}{[\mathbf{r}_l^i + \mathbf{T}_b^i \mathbf{r}_a^b - \mathbf{T}_p^i \mathbf{r}_{gs}^p]} + b_{\dot{\rho}} + v_{\dot{\rho}} \quad (19)$$

The uncertainty parameters used for the DSN ground updates are given in Table 2.

OpNav The optical navigation (OpNav) system produces bearing measurements to the centroid of a celestial body, both a horizontal α_h and vertical α_v , along with a range measurement ρ based on the apparent angular diameter of the planet. OpNav measurements are functions of the centroid and apparent angular biases b , noise η , and pointing error. Rather than processing the *raw* angles, the tangent of the angles are utilized, \tilde{y}_h and \tilde{y}_v .²² Conceptually, the core measurements are

$$\tilde{y}_h = \tan(\alpha_h) + b_h + \eta_h = x/z + b_h + \eta_h \quad (20)$$

$$\tilde{y}_v = \tan(\alpha_v) + b_v + \eta_v = y/z + b_v + \eta_v \quad (21)$$

$$\tilde{\rho} = \rho + b_\rho + \eta_\rho = \sqrt{x^2 + y^2 + z^2} + b_\rho + \eta_\rho \quad (22)$$

where $\boldsymbol{\rho}^T = (\mathbf{r}_o - \mathbf{r}_p)^T = [x, y, z]$ and the *range* measurement $\tilde{\rho}$ is actually converted to an apparent angular diameter and all the measurements are processed in terms of pixels. The parameters used for the OpNav system are provided in Table 6. The uncertainty of OpNav measurements depend on the celestial body, range to celestial body, and camera specifications.

The OpNav field of view (FOV) constraint shown in Table 6 is dependent on camera properties and equal to 20 degrees. If the apparent angular diameter of the target celestial body exceeds the FOV constraint, no OpNav measurements are taken. Lighting constraints were not activated for this study. Lastly, to ensure that navigation never goes more than a day without a lunar OpNav measurement, an Opnav pass is always inserted between two burns when they are separated by more than 24 hours.

Accelerometer The accelerometer measures the non-gravitational acceleration in the IMU case frame $\tilde{\mathbf{a}}^{imu}$, which is a function of the nominal inertial-to-body transformation matrix $\bar{\mathbf{T}}_i^b$, the nominal body-to-IMU transformation $\bar{\mathbf{T}}_b^{imu}$, the actual attitude dispersion $\boldsymbol{\theta}$, the misalignment $\boldsymbol{\mu}_a$, the constant scale factor s_a , the Markov scale factor $\boldsymbol{\sigma}_a$, the constant bias \mathbf{b}_a , the Markov bias $\boldsymbol{\beta}_a$, the nonorthogonality factor γ_a , and the velocity random walk (noise) \mathbf{v}_a .

$$\tilde{\mathbf{a}}^{imu} = (\mathbf{I} + [(\mathbf{s}_a + \boldsymbol{\sigma}_a)\setminus]) \left[(\mathbf{I} + [\boldsymbol{\mu}_a \times]) (\mathbf{I} + [\gamma_a *]) \bar{\mathbf{T}}_b^{imu} (\mathbf{I} + [\boldsymbol{\theta} \times]) \bar{\mathbf{T}}_i^b \mathbf{a}^i + \mathbf{b}_a + \boldsymbol{\beta}_a + \mathbf{v}_a \right] \quad (23)$$

The uncertainty parameters used for the accelerometer are listed in Table 3.

Gyro The gyros measure the vehicle's angular rates in the IMU case frame $\tilde{\boldsymbol{\omega}}^{imu}$ and is represented as a function of the nominal body-to-IMU transformation $\bar{\mathbf{T}}_b^{imu}$ where b indicates the vehicle body-fixed frame, the misalignment $\boldsymbol{\mu}_\omega$, the constant scale factor s_ω , the Markov scale factor $\boldsymbol{\sigma}_\omega$, the constant bias \mathbf{b}_ω , the Markov bias $\boldsymbol{\beta}_\omega$, the nonorthogonality factor γ_ω , and the angular random walk (noise) \mathbf{v}_ω

$$\tilde{\boldsymbol{\omega}}^{imu} = (\mathbf{I} + [(\mathbf{s}_\omega + \boldsymbol{\sigma}_\omega)\setminus]) \left[(\mathbf{I} + [\boldsymbol{\mu}_\omega \times]) (\mathbf{I} + [\gamma_\omega *]) \bar{\mathbf{T}}_b^{imu} \boldsymbol{\omega}^b + \mathbf{b}_\omega + \boldsymbol{\beta}_\omega + \mathbf{v}_\omega \right] \quad (24)$$

The uncertainty parameters used for the gyroscope are listed in Table 4.

Star Tracker The star tracker provides an accurate measurement of the vehicle's orientation. The generated inertial-to-star tracker quaternion is a function of the body-to-star tracker mounting \mathbf{q}_b^{st} , the actual inertial-to-body quaternion \mathbf{q}_i^b , the sensor bias \mathbf{b}_{st} , noise $\boldsymbol{\eta}_{st}$, and misalignment $\boldsymbol{\mu}_{st}$

$$\tilde{\mathbf{q}}_{st}^i = \mathbf{q}(\boldsymbol{\eta}_{st}) \otimes \mathbf{q}(\mathbf{b}_{st}) \otimes \mathbf{q}(\boldsymbol{\mu}_{st}) \otimes \mathbf{q}_b^{st} \otimes \mathbf{q}_i^b \quad (25)$$

The star tracker parameters are summarized in Table 5.

Table 2. DSN Update

Parameter	3σ
Range Noise, m	25
Range-rate Noise, cm/s	1.5
Range Bias, m	25
Range-rate Bias, cm/s	1.5
Elevation Mask, deg	10.0
Max Pass Duration, hr	2.0

Table 3. Accelerometer²³

Parameter	3σ
VRW, mm/s/sqrt(s)	0.3
Bias, μg	84
Scale Factor, ppm	450
Nonorthogonality, arcsec	17
Markov Bias, μg	84
Markov Scale Fact, ppm	450

Table 4. Gyros²³

Parameter	3σ
ARW, deg/\sqrt{hr}	0.015
Bias, deg/hr	0.036
Scale Factor, ppm	27
Nonorthogonality, arcsec	19
Markov Bias, deg/hr	0.036
Markov Scale Factor, ppm	27

Table 5. Startracker²³

Parameter	3σ
Boresight Noise, arcsec	72
Crs-Boresight Bias, arcsec	24
Misalignment, deg	0.5

Table 6. OpNav

Parameter	3σ
Body (NAIF ID)	301/399
Pass Duration, hr	2
FOV, deg	20

Table 7. Process Noise

Parameter	3σ
Trans (LEO), m/\sqrt{s}	—
Trans (Cis-lunar), m/\sqrt{s}	—
Rotational, rad/\sqrt{s}	$0.0e^{-6}$

Table 8. Initial Dispersions

Parameter	3σ
Position, km	2
Velocity, cm/s	20
Attitude, deg	0.5
Attitude-Rate, deg/s	0.01

Table 9. Initial Navigation

Parameter	3σ
Position, km	2
Velocity, cm/s	2
Attitude, deg	0.05
Attitude-Rate, deg/s	0.01

Table 10. Thrusters

Parameter	3σ
Bias, cm/s	8
Noise, cm/s	8
Scale Factor, ppm	7000
Misalignment, deg	0.1

Translational Burn Modeling

All the major translational burns and the correction burns are assumed to be impulsive and are executed using a two-level targeter^{24,25,26,27,28} (TLT) that targets the EI parameters and lunar radius of periapses. The algorithm works by dividing the trajectory into segments or a series of intermediate targets known as patch states. The first stage, or the level-I process, introduces impulsive maneuvers at the interior patch states until position continuity across all segments is achieved. The second stage, or the level-II process, adjusts the shape of the trajectory by spatially and temporally relocating the patch states to drive the velocity discontinuities to zero. This approach is not limited to merely targeting a terminal position vector, but any terminal constraint such as flight path angle, altitude, velocity magnitude, or any function of the position and velocity state. All the impulsive burns have execution errors due to thruster misalignment, scale factor, bias, and noise. Table 10 lists each thruster error model component.

Disturbance Acceleration Modeling

Artemis II will be the first mission to have crew to fly the Orion spacecraft. As a result, there are additional disturbance accelerations due to the Environmental Control and Life Support System (ECLSS) that provides clean air and water to the crew. The ECLSS perturbations include pressure swing adsorption (PSA) during crew sleep, awake, and active periods, waste water vents, and ammonia sublimator. The non-ECLSS perturbations include attitude dead-banding maneuvers, attitude slew maneuvers, and solar radiation pressure. A summary of previously derived process noise values¹⁸ Q for Artemis II is provided below in Table 11.

Table 11. Artemis II ECLSS and Non-ECLSS Disturbance Accelerations

Event	Process Noise	Q (ft ² /s ³)	Duration
ECLSS	Pressure Swing Adsorption (Sleep)	2.9859×10^{-8}	During sleep periods only
	Pressure Swing Adsorption (Awake)	9.4313×10^{-8}	During non-exercise awake periods
	Pressure Swing Adsorption (Active)	6.4741×10^{-7}	During crew exercise periods only
	Waste Water Vents	4.9546×10^{-7}	8.6 min, 4 times a day
	Ammonia Boiler	8.5488×10^{-5}	45 min, 1 hour prior EI
Non-ECLSS	Attitude Dead-banding Maneuvers	3.4319×10^{-13}	During entire on-orbit phase
	Attitude Slew Maneuvers	1.2122×10^{-10}	During entire on-orbit phase
	Solar Radiation Pressure	8.9704×10^{-14}	During entire on-orbit phase

A subtle yet important aspect of the ECLSS impact study is characterizing how the process noise reflecting the disturbance accelerations due to the ECLSS events are modeled. There are several options of modeling the disturbance accelerations due to venting highlighted in Figure 7. The first assumes a generic three-axis venting direction with the ECLSS disturbance accelerations averaged out over the entire profile such that a single process noise value is incorporated in all three body axes. The second also assumes a generic three axis direction with the ECLSS disturbance accelerations but they are scheduled at their specified time intervals. The third approach models a specific venting direction in the Orion structural frame at their specified time intervals which requires the Orion vehicle attitude to be defined throughout the entire scenario.

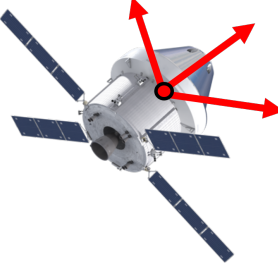

Generic 3-Axis Venting Direction	Specific Venting Direction
<p>The derived disturbance acceleration uncertainty magnitude is assumed to be in all three orthogonal axes regardless of the actual number and vent direction. Independent of Orion's attitude.</p> 	<p>The derived disturbance acceleration uncertainty magnitude is assumed to be aligned with the actual ECLSS vent direction and only in that direction. Dependent on Orion's attitude.</p> 

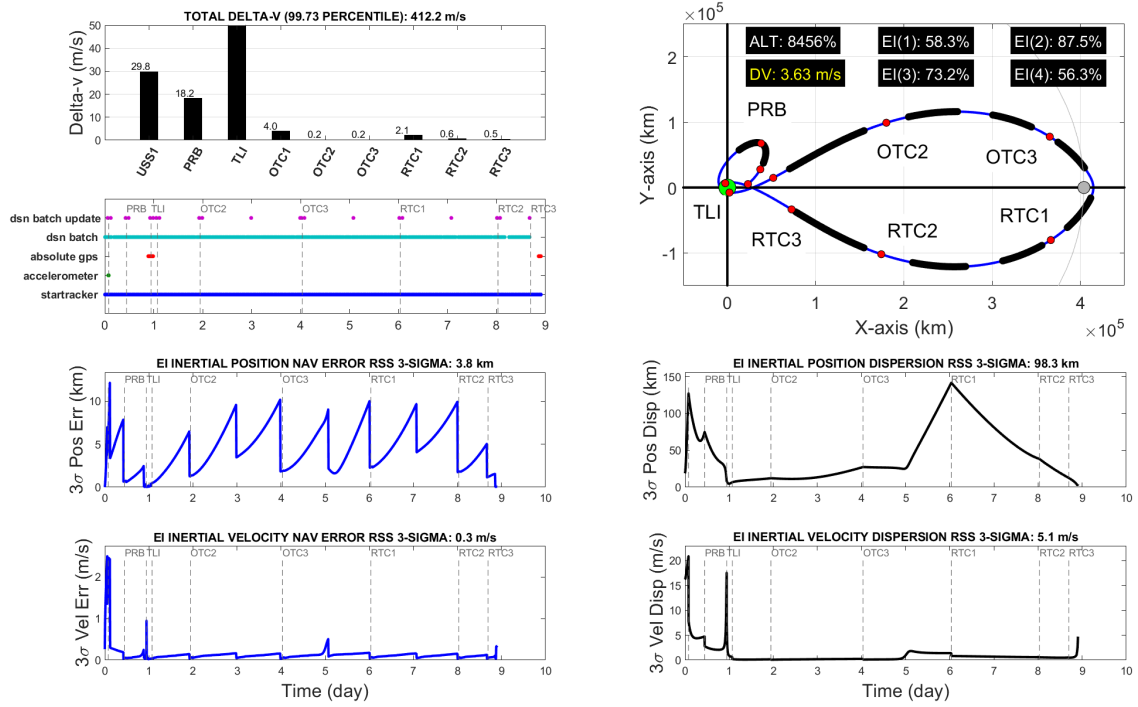
Figure 7. Artemis II Venting Modeling Approaches

For this analysis, since the vehicle orientation is not formally defined for the end-to-end mission yet, the ECLSS modeling adopts the second option such that the vehicle attitude profile does not impact the resulting disturbance accelerations due to venting, but the magnitude of the disturbance accelerations varies and is scheduled to reflect the frequency, number, and duration of each ECLSS event as outlined in Table 11. This approach is slightly conservative, but relevant.

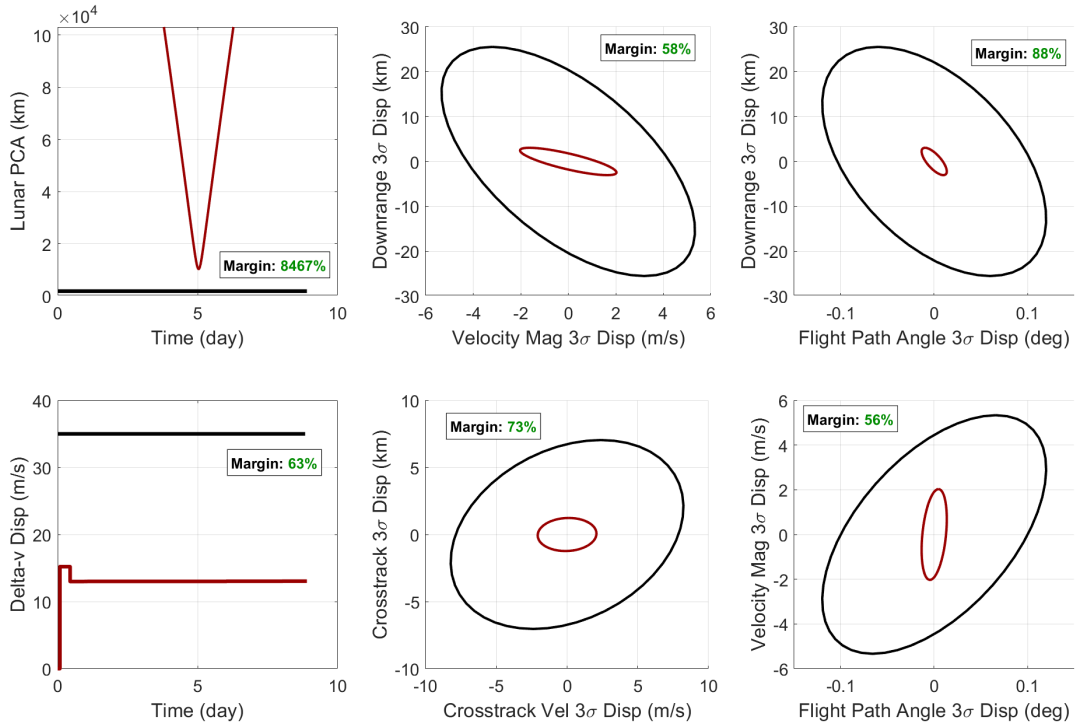
OPTIMIZED ARTEMIS II TRAJECTORY CORRECTION BURN PLACEMENT

Given the robust trajectory optimization techniques and parameters introduced previously, along with the concept of operations for the Artemis II mission and the assumptions regarding the GN&C system modeling, this section derives optimized placement of the notional Artemis II outbound and return trajectory correction burns. To provide a comparison, the non-optimized results from the baseline scenario in Table 1 are captured using three different navigation configurations: 1) Perfect Nav, 2) DSN, and 3) OpNav. Then optimized trajectory correction burn placements are derived for each navigation configuration for the three different objective functions: Problem #1) minimize the total delta-v with a final EI dispersion constraint, Problem #2) minimize the EI dispersions subject to a total delta-v constraint, and Problem #3) minimize both total delta-v and the EI dispersions simultaneously.

The performance results for the baseline trajectory correction burn placement using DSN is provided in Figure 8. Figure 8(a) highlights details regarding the total delta-v (top left plot) along with measurement scheduling, inertial position and velocity navigation errors, the reference trajectory with the simulated burn placement, and the inertial position and velocity trajectory dispersions. Figure 8(b) summarizes the performance compliance with the top-level requirements defined previously which includes the lunar flyby altitude, total delta-v dispersions, and the entry interface



(a) Overview of Trajectory Performance



(b) Compliance with Top-Level Performance Requirements

Figure 8. DSN Baseline Results

requirements. Rather than showing this complete data set for each optimized scenario, only the plot in the top-right quadrant of Figure 8(a) is provided which includes the geometrical placement of the optimized trajectory correction burns and the resulting lunar flyby altitude dispersion margin (8,456%), total delta-v for OTC2 to RTC3 correction burns, $DV = 3.63$ m/s, and the EI percent margin for downrange and velocity magnitude, $EI(1) = 58.3\%$, downrange and flight path angle dispersions, $EI(2) = 87.5\%$, crosstrack position and velocity dispersions, $EI(3) = 73.2\%$, and velocity magnitude and flight path angle dispersions, $EI(4) = 56.3\%$.

Non-Optimized Performance Results for Baseline Trajectory Correction Burn Placement

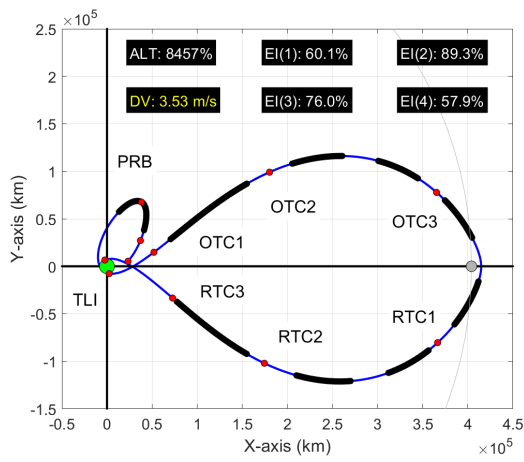
Figure 9 provides a summary of the performance for the baseline trajectory correction burn placement for the different navigation configurations of Perfect Nav, DSN, and OpNav. The first row of plots captures the performance using Perfect Nav where Figure 9(a) summarizes the results for the baseline burn placement and Figure 9(b) shows specific details related to the actual EI dispersions (maroon ellipse) with respect to the requirements (solid black ellipse). The total delta-v is 3.53 m/s from OTC2 to RTC3. The EI dispersion percent margin varies from 58% to 89%. The second row of plots in Figure 9(c) and Figure 9(d) shows the baseline DSN results emphasized earlier where the total delta-v only has a 0.1 m/s degradation compared to the Perfect Nav case and the EI dispersions margin drops only by 2-3%.

The last row of plots in Figure 9(e) and Figure 9(f) gives the OpNav performance results. Compared to both the Perfect Nav and DSN scenarios, the OTC and RTC burns require a delta-v of 12.3 m/s which is about three times more. The EI dispersions for OpNav given the baseline burn placement has the most noticeable degradation. The requirements between the primary (DSN) and backup (OpNav) systems are different by a factor of 2.5 where the 2-sigma values are used instead of the 3-sigma values. The percent margin comparison has the greatest discrepancy in the flight path angle dispersions with the percent margin for $EI(2)$ decreasing in half. The question now to answer is can both the total delta-v and the EI trajectory dispersions be improved for all cases by optimizing the placement of each burn? If so, what level of improvement can be achieved?

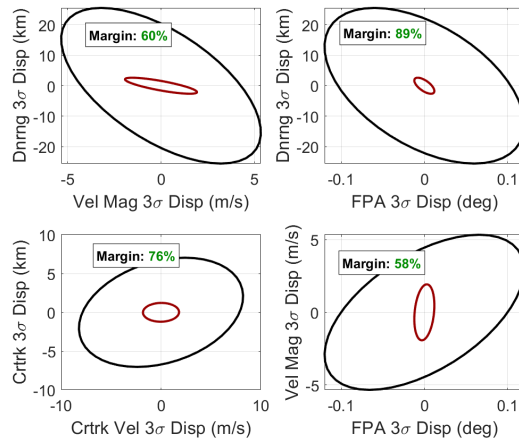
Problem #1: Optimized Correction Burn Placement to Minimize Total Delta-v

Figure 10 summarizes the optimized trajectory burn placement and performance utilizing the objective function in Problem #1 where the total delta-v for OTC2 through RTC3 is minimized with a constraint on satisfying the EI dispersion requirements for the three different navigation systems including Perfect Nav, DSN, and OpNav shown with the plots in rows 1, 2, and 3 respectively. The plots on the left column show the optimized burn placement when the crew schedule is not accounted for in the design process. The plots on the right column account for the crew schedule by prohibiting any trajectory correction burn during this period.

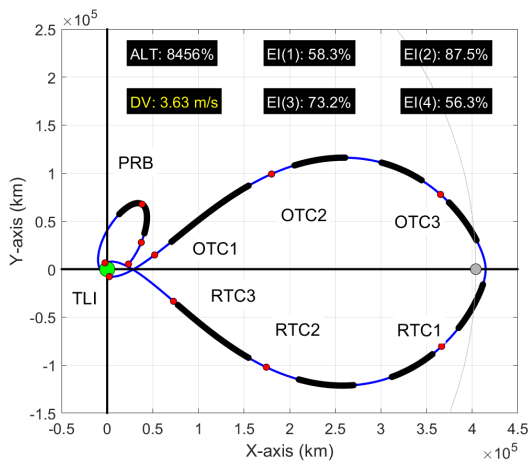
A few quick observations. The total delta-v from OTC2 to RTC6 can be reduced by almost a factor of 2 (or 1.5 m/s) for both the Perfect Nav and DSN cases by shifting RTC3 prior to the last crew sleep period and executing RTC1 just after lunar flyby but prior to ensuing crew sleep period. A noticeable degradation in the EI dispersions results from this shift in burn placement, but there is still an EI performance margin from 25% to 70%. For OpNav, in order to satisfy the EI dispersion constraints, the minimum delta-v is found by placing RTC3 following the last crew sleep period as is done in the baseline and placing RTC1 following the crew sleep period after the lunar flyby (rather than before). For OpNav, optimizing the burn placement can improve the total delta-v performance by 2-5 m/s.



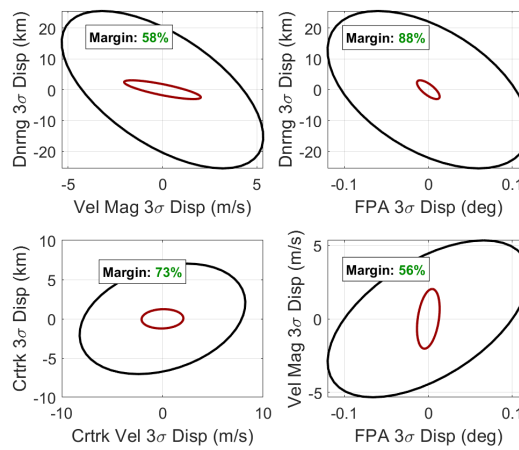
(a) BASELINE: Perf Nav Summary



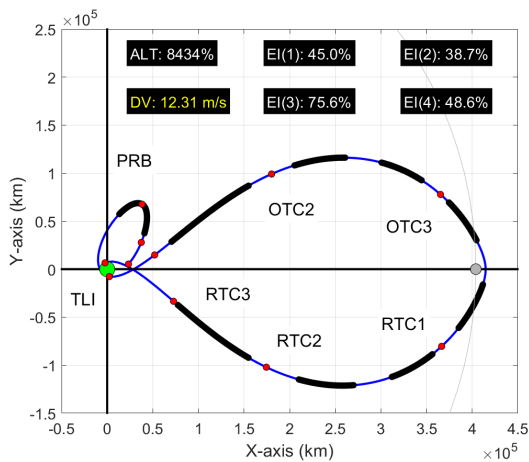
(b) BASELINE: Perf Nav EI Dispersions



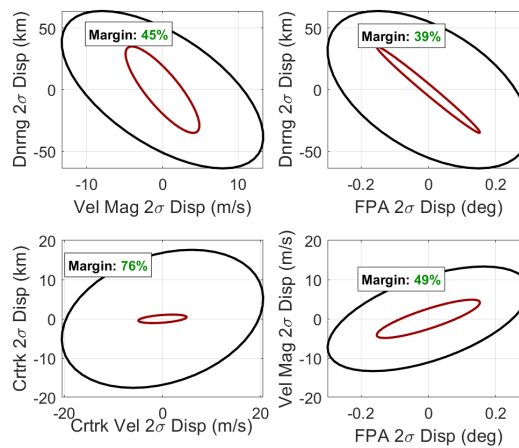
(c) BASELINE: DSN Nav Summary



(d) BASELINE: DSN Nav EI Dispersions

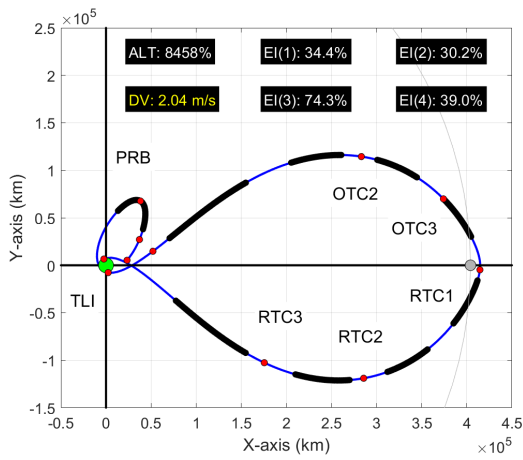


(e) BASELINE: OpNav Summary

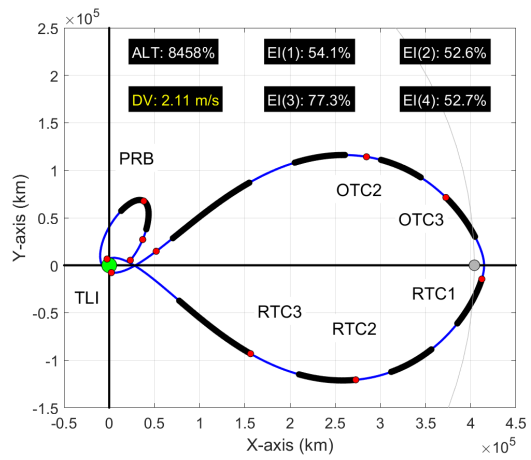


(f) BASELINE: OpNav EI Dispersions

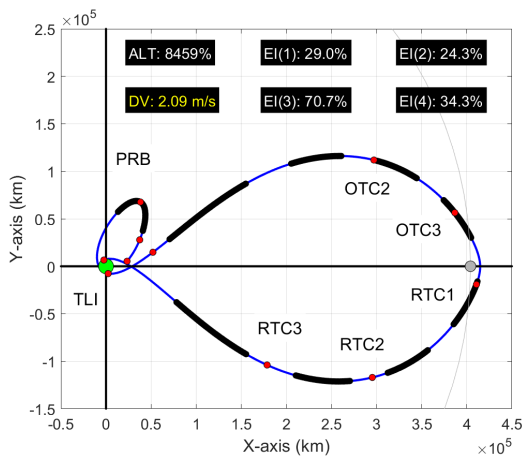
Figure 9. Problem #1 (Minimize Dv): Optimized Trajectory Burn Placement



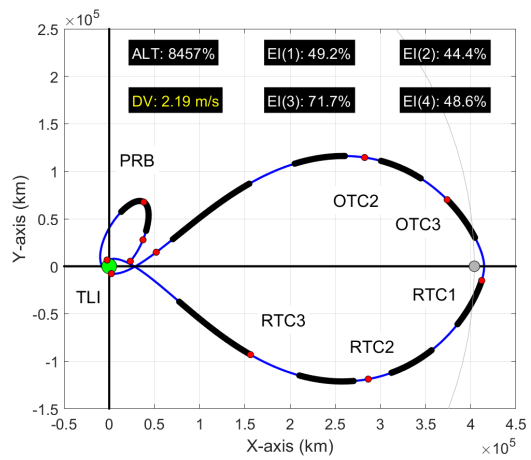
(a) P1: PERFECT NAV, NO CREW SCHEDULE



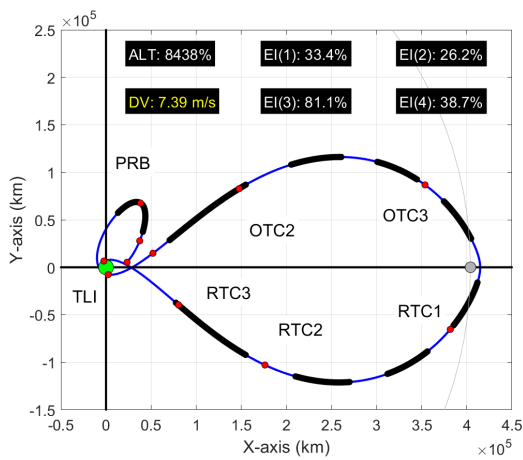
(b) P1: PERFECT NAV, CREW SCHEDULE



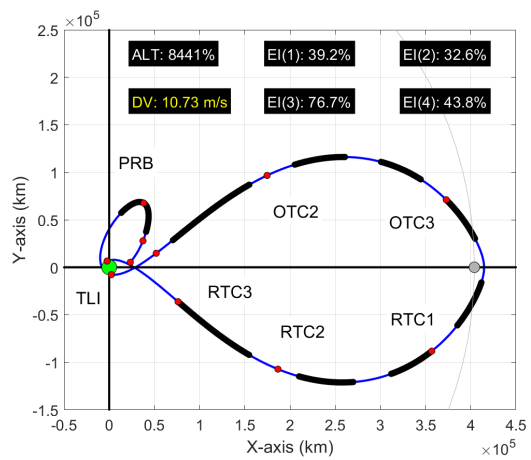
(c) P1: DSN NAV, NO CREW SCHEDULE



(d) P1: DSN NAV, CREW SCHEDULE

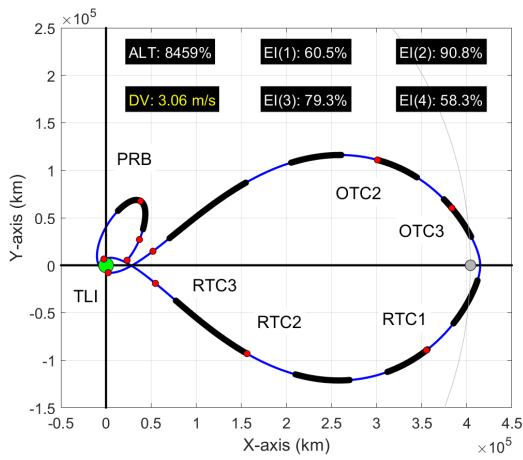


(e) P1: OPNAV, NO CREW SCHEDULE

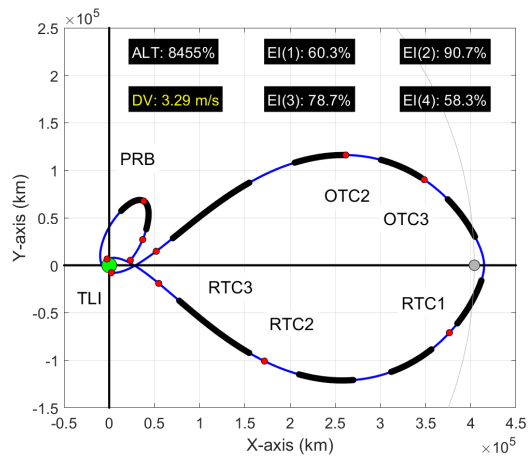


(f) P1: OPNAV, CREW SCHEDULE

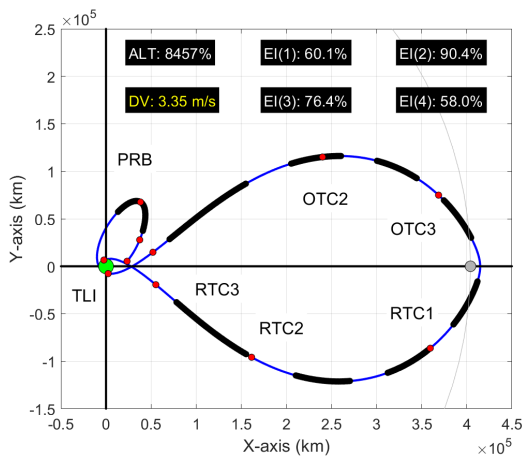
Figure 10. Problem #1 (Minimize Dv): Optimized Trajectory Burn Placement



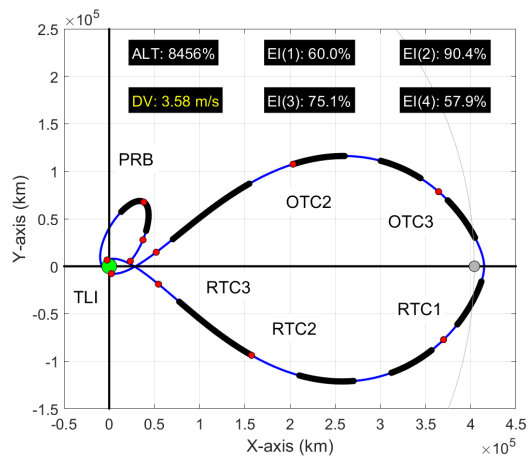
(a) P2: PERFECT NAV, NO CREW SCHEDULE



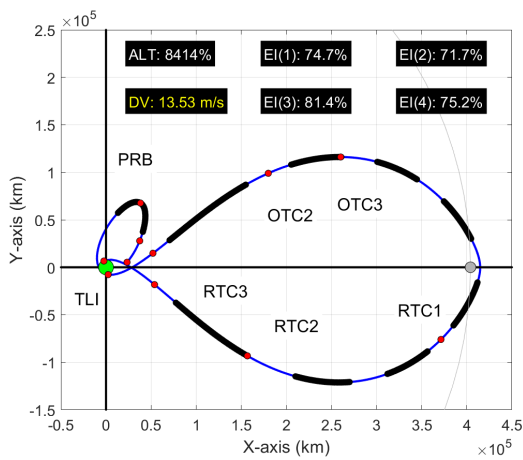
(b) P2: PERFECT NAV, CREW SCHEDULE



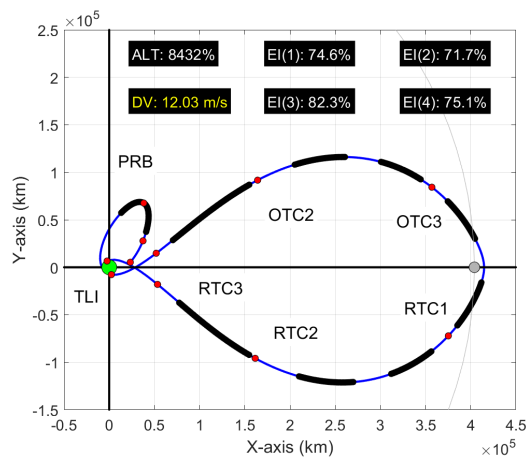
(c) P2: DSN NAV, NO CREW SCHEDULE



(d) P2: DSN NAV, CREW SCHEDULE

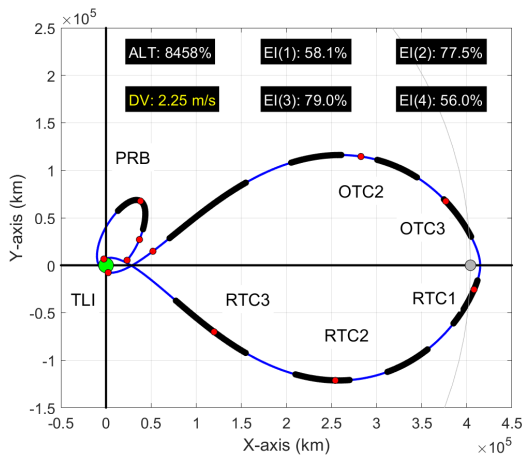


(e) P2: OPNAV, NO CREW SCHEDULE

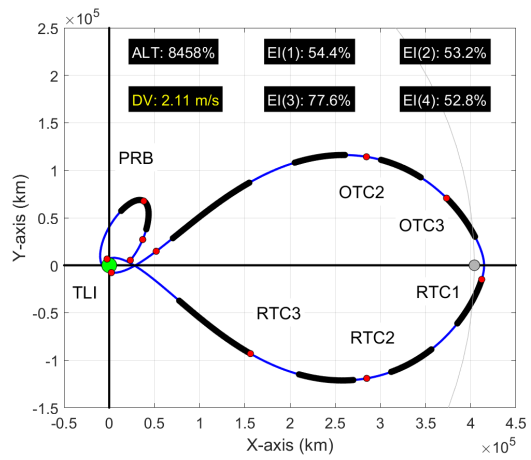


(f) P2: OPNAV, CREW SCHEDULE

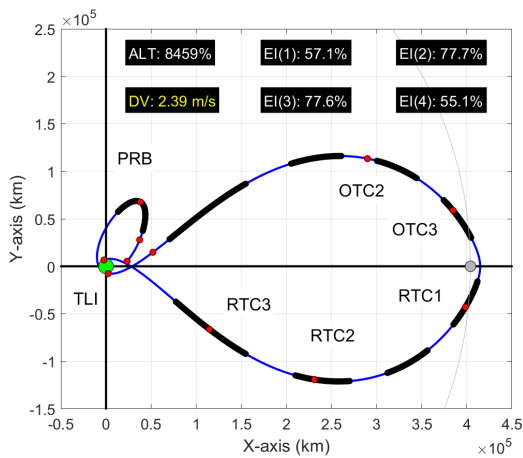
Figure 11. Problem #2 (Minimize ED): Optimized Trajectory Burn Placement



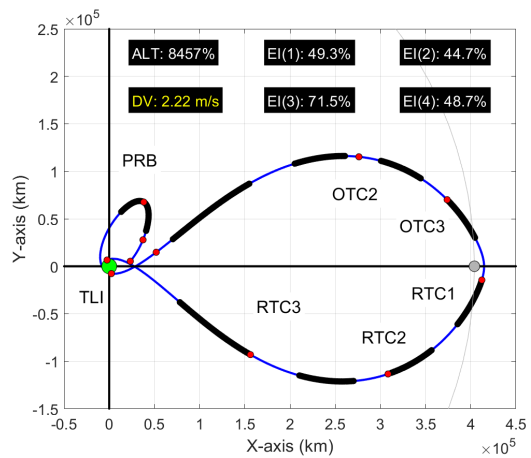
(a) P3: PERFECT NAV, NO CREW SCHEDULE



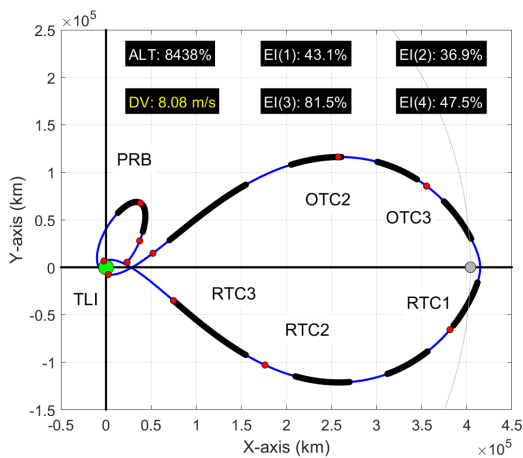
(b) P3: PERFECT NAV, CREW SCHEDULE



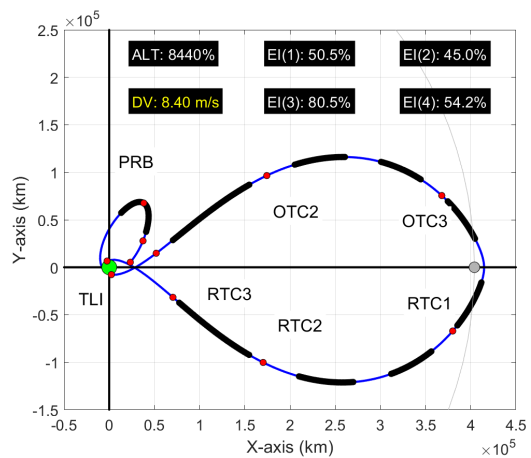
(c) P3: DSN NAV, NO CREW SCHEDULE



(d) P3: DSN NAV, CREW SCHEDULE



(e) P3: OPNAV, NO CREW SCHEDULE



(f) P3: OPNAV, CREW SCHEDULE

Figure 12. Problem #3 (Minimize Dv and EI): Optimized Trajectory Burn Placement

Problem #2: Optimized Correction Burn Placement to Minimize EI Dispersions

Figure 11 highlights the optimized burn placement when minimizing EI dispersions as specified with the objective function in Problem #2 where total delta-v for OTC2 through RTC3 must not exceed the allocated limit of 20 m/s. Regardless of the navigation system utilized, the common trend to minimize EI dispersions is to perform RTC3 as late as possible. For all cases the optimizer pushes RTC3 to occur 3 hours prior to EI, which was the limit allocated in the assumptions. For RTC2, each scenario also placed it shortly before the last crew sleep period prior to EI. RTC1 typically occurs following the crew sleep period after lunar flyby. Compared to the baseline, the total delta-v is nearly the same and occasionally slightly less even when optimizing for the EI dispersions. However, the EI dispersions performance margin increases and most noticeably with OpNav where the margin goes from 40% to 75% for baseline to 75% to 80% with the optimized placement.

Problem #3: Optimized Correction Burn Placement to Minimize Delta-v and EI Dispersions

Figure 12 shows the optimized burn placement when simultaneously striving to minimize both total delta-v and EI dispersions based on the objective function defined in Problem #3. The solutions emerging from this problem formulation reflect the results from Problem #1 where efforts were made to minimize the total delta-v. For this particular setup, the delta-v performance margin was weighted higher than the EI dispersion with a weighting factor of 0.75 for delta-v and 0.25 for EI dispersions. Ultimately, the priorities of the program will determine the proper weighting factors and placement selection for the trajectory correction burns.

CONCLUSION

This work attempts to provide preliminary performance results that identify optimized trajectory correction burn placement using non-traditional robust trajectory optimization techniques for the upcoming NASA Artemis II mission. By combining linear covariance analysis and a genetic algorithm, uncertainty in the system can be accommodated and trajectory correction burns which are nominally zero, can be strategically placed to reduce total delta-v (nominal + 3-sigma dispersions) while ensuring the vehicle satisfies entry interface dispersion requirements and does not violate lunar altitude flyby constraints. Arbitrarily selecting the number and placement of the trajectory correction burns following the trans-lunar injection burn can lead to a significant increase of delta-v and violation of entry interface requirements. The sensitivity to burn placement as a function of the navigation system and the selected optimization objective functions is also provided.

REFERENCES

- [1] P. S. Maybeck, *Stochastic models, estimation, and control*, Vol. 1. New York: Academic Press, 1979.
- [2] D. K. Geller, "Linear Covariance Techniques for Orbital Rendezvous Analysis and Autonomous On-board Mission Planning," *Journal of Guidance, Control, and Dynamics*, Vol. 29, November-December 2006, pp. 1404–1414.
- [3] K. Jin, D. K. Geller, and J. Luo, "Robust Trajectory Design for Rendezvous and Proximity Operations with Uncertainties," *Journal of Guidance, Control, and Dynamics*, Vol. 43, No. 4, 2020, pp. 741–753.
- [4] D. K. Geller, S. Shuster, D. Woffinden, and S. Bieniawski, "Robust Cislunar Trajectory Optimization via Midcourse Correction and Optical Navigation Scheduling," *44th Annual AAS Guidance, Navigation and Control Conference*, Breckenridge, CO, AAS 22-065, 4-9 February 2022 2022.
- [5] D. Woffinden, S. Shuster, and S. Geller, David Kand Bieniawski, "Robust Trajectory Optimization and GN&C Performance Analysis For NRHO Rendezvous," *2022 AAS/AIAA Astrodynamics Specialist Conference*, Charlotte, North Carolina, 22-564, 7-11 August 2022 2022.

- [6] D. Geller, D. Woffinden, and S. Bieniawski, "Sensitivity of Optimal Midcourse Correction Scheduling for Robust Cislunar Trajectory Design," *45th Rocky Mountain AAS GN&C Conference*, Breckenridge, CO, AAS 23-061, 2 Feb - 8 Feb 2023.
- [7] T. Goulet, D. Woffinden, N. Collins, and B. Andrews, "Robust Trajectory Design for Rendezvous in a Near Rectilinear Halo Orbit," *45th Rocky Mountain AAS GN&C Conference*, Breckenridge, CO, AAS 23-066, 2 Feb - 8 Feb 2023.
- [8] G. Calkins, D. Woffinden, and Z. Putnam, "Robust Trajectory Optimization for Guided Powered Descent and Landing," *2022 AAS/AIAA Astrodynamics Specialist Conference*, Charlotte, NC, AAS 22-660, 7-11 August 2022 2022.
- [9] J. Joshi, D. Woffinden, and Z. Putnam, "End-to-End Mars Aerocapture Analysis Using Linear Covariance Techniques and Robust Trajectory Optimization," *2022 AAS/AIAA Astrodynamics Specialist Conference*, Charlotte, NC, AAS 22-678, 7-11 August 2022 2022.
- [10] D. Woffinden and B. Barton, "Optimized Trajectory Correction Burn Placement for NRHO Orbit Maintenance," *33rd AAS/AIAA Space Flight Mechanics Meeting*, Austin, TX, AAS 23-364, 15 - 19 January 2023.
- [11] T. J. Moesser and D. K. Geller, "Guidance and Navigation Linear Covariance Analysis for Lunar Powered Descent," *AAS/AIAA Astrodynamics Specialist Conference*, Mackinac Island, Michigan, AAS 07-313, 19-23 August 2007.
- [12] D. Geller and D. Christensen, "Linear Covariance Analysis for Powered Lunar Descent and Landing," *The Journal of Spacecraft and Rockets*, Vol. 46, Nov-Dec 2009, pp. 1231–1248.
- [13] D. Woffinden, S. Robinson, J. Williams, and Z. Putnam, "Linear Covariance Analysis Techniques to Generate Navigation and Sensor Requirements for the Safe and Precise Landing - Integrated Capabilities Evolution (SPLICE) Project," *AIAA Scitech 2019 Forum*, San Diego, CA, AIAA 2019-0662, 7-11 January 2019 2019.
- [14] J. W. Williams, W. E. Brandenburg, D. C. Woffinden, and Z. R. Putnam, "Validation of Linear Covariance Techniques for Mars Entry, Descent, and Landing Guidance and Navigation Performance Analysis," *AIAA Scitech 2022 Forum*, 2022, 10.2514/6.2020-0597.
- [15] J. Rea, "Entry Interface Accuracy Requirements for Exploration Mission Critical Design Review," Tech. Rep. FltDyn-CEV-15-28, National Aeronautics and Space Administration, Johnson Space Center, Engineering Directorate, July 2015.
- [16] R. Zanetti and C. DSouza, "Navigation and Dispersion Analysis of the First Orion Exploration Mission," *39th Annual AAS Guidance and Control Conference*, Breckenridge, CO, AAS 15-758, 5-10 Feb 2015.
- [17] C. DSouza, G. Holt, R. Zanetti, and B. Wood, "Ground-Based Navigation and Dispersion Analysis for the Orion Exploration Mission 1," *39th Annual AAS Guidance and Control Conference*, Breckenridge, CO, AAS 16-235, 5-10 Feb 2016.
- [18] C. D'Souza and R. Zanetti, "Navigation Design and Analysis for the Orion Exploration Mission 2," *AAS/AIAA Astrodynamics Specialist Conference*, Stevenson, WA, AAS 17-643, 20-24 Aug 2017.
- [19] D. Woffinden, S. Bhatt, D. Kirkpatrick, and P. Spanos, "Optimal Multi-Variable Multi-Constraint Spacecraft GN&C Requirement Derivation," *41st Annual AAS Guidance and Control Conference*, Breckenridge, CO, AAS 18-095, 5-10 Feb 2018.
- [20] M. Mitchell, *An Introduction to Genetic Algorithms*. 1996.
- [21] B. C. Collicott and D. C. Woffinden, *Lunar Navigation Performance using the Deep Space Network and Terrain Relative Navigation to Support Precision Landing*. 19-21 January 2021, 10.2514/6.2021-0375.
- [22] G. N. Holt, C. N. D'Souza, and D. Saley, "Orion Optical Navigation Progress Toward Exploration Mission 1," *AIAA Scitech 2018 Forum, Space Flight Mechanics Meeting*, Kissimmee, Florida, AIAA 2018-1978, 8-12 January 2018 2018.
- [23] A. M. Dwyer-Cianciolo, C. D. Karlgaard, D. Woffinden, R. A. Lugo, J. Tynis, R. R. Sostaric, S. Striepe, R. Powell, and J. M. Carson, "Defining Navigation Requirements for Future Missions," *AIAA Scitech 2019 Forum*, San Diego, 2019. 2019-0661, 10.2514/6.2019-0661.
- [24] B. G. Marchand, K. Howell, and R. Wilson, "Improved Corrections process for Constrained Trajectory Design in the n Body Problem," *Journal of Spacecraft and Rockets*, Vol. 35, July 2007, pp. 1–33, 10.2514/1.27205.
- [25] M. W. Weeks, B. G. Marchand, C. W. Smith, and S. Scarritt, "Design of the Onboard Autonomous Targeting Algorithm for the Trans-Earth Phase of Orion," Honolulu, Hawaii, AIAA Guidance, Navigation and Control Conference and Exhibit, 18-21 August 2008.
- [26] B. G. Marchand, M. W. Weeks, C. W. Smith, and S. Scarritt, "Onboard Autonomous Targeting for the Trans-Earth Phase of Orion," *Journal of Guidance, Control, and Dynamics*, Vol. 33, May-June 2010, pp. 943–956, 10.2514/1.42384.

- [27] S. Scarritt, B. G. Marchand, A. J. Brown, W. H. Tracy, and M. W. Weeks, "Finite-Burn Linear Targeting Algorithm for Autonomous Path Planning Guidance," *Journal of Guidance, Control, and Dynamics*, Vol. 35, September-October 2012, pp. 1605–1615, 10.2514/1.54249.
- [28] S. K. Scarritt, T. Fill, and S. Robinson, "Advances in Orion's On-Orbit Guidance and Targeting System Architecture," Breckenridge, CO, AAS 15-096, 1 Feb - 6 Feb 2015.